REVIEW

Check for updates

Precursor chemistry of metal nitride nanocrystals

Mahsa Parvizian [ID] and Jonathan De Roo [ID] *

Metal nitride nanocrystals are a versatile class of nanomaterials. Depending on their chemical composition, the optical properties vary from those of traditional semiconductor nanocrystals (called quantum dots) to more metallic character (featuring a plasmon resonance). However, the synthesis of colloidal metal nitride nanocrystals is challenging since the underlying precursor chemistry is much less developed compared to the chemistry of metal, metal chalcogenide or metal phosphide nanocrystals. Here, we review chemical approaches that lead (or could lead) to the formation of colloidally stable metal nitride nanocrystals. By systematically comparing different synthetic approaches, we uncover trends and gain insight into the chemistry of these challenging materials. We also discuss and critically evaluate the plausibility of certain suggested mechanisms. This review is meant as a guide for the further development of colloidal nitride nanocrystals.

Department of Chemistry, University of Basel, Basel, Switzerland.
E-mail: Jonathan.DeRoo@unibas.ch; Tel: +41 61 207 10 46

1. Introduction

Various nanomaterials show size-dependent properties, *e.g.*, magnetic, electrical, and optical properties that cannot be achieved in the bulk material. Therefore, the synthesis of uniform nanocrystals (NC) with controlled size and shape has been attracting a lot of attention.[1] While atomic precision is still more an aspiration than a reality in nanocrystal science,[2] it is imperative to produce colloids with narrow size distri-

butions (low polydispersity) to allow the study of size dependent properties.[3] One of the most well-known phenomena is the tunable luminescence of quantum dots (QDs), covering the entire UV-VIS-NIR spectrum depending on the QD size and chemical composition.[4]

Ligand-assisted, wet chemical synthesis has provided the necessary control over nanocrystal size and shape.[5] However, it is a complex process, combining metal–organic chemistry, inorganic crystallization and surface chemistry to yield an organic/inorganic hybrid object that is colloidally stable. The precursor conversion mechanism of many metals, metal chalcogenide, metal phosphide and metal halide NCs has been elucidated.[6–9]

Mahsa Parvizian completed her Bachelor and Master in chemistry at the University of Paris. In 2020 she started her PhD under the supervision of Prof. De Roo at the University of Basel. Her research focuses on the synthesis of metal nitride nanocrystals and their reaction mechanism.

Mahsa Parvizian

Dr Jonathan De Roo studied chemistry at Ghent University and obtained his PhD on the surface chemistry of metal oxide nanocrystals in 2016. During his PhD, he was also three months at ETH Zurich to study the surface of CsPbBr$_3$ nanocrystals. He completed a postdoc at Columbia University, working on crystallization mechanisms and the design of new ligands. In 2019, he joined the University of Basel as Tenure Track Assistant

Jonathan De Roo

Professor. His research team focuses on mechanistic aspects in the synthesis of ceramic nanocrystals and atomically precise oxo-clusters. Both precursor conversion and crystallization mechanism are studied.

and also their surface chemistry is increasingly better understood.[10–16] The crystallization mechanism (*i.e.*, nucleation and growth) causes more discussion in the literature.[17,18] Approaches based on classical nucleation theory are at odds with the Finke–Watzky based mechanisms.[19,20] Recent evidence shows that many NCs do not nucleate *via* a burst nucleation event, but rather that nucleation is a continuous process.[21–23] Continuous nucleation does not necessarily lead to polydisperse ensembles because small NCs grow faster than larger NCs, allowing the newly formed NCs to catch up with the growing NC population.[22–25] Even without a comprehensive framework for NC crystallization, chemists have been able to adjust the final NCs size by controlling the precursor conversion rate.[26] The three aspects of colloidal synthesis (precursor conversion, crystallization and surface chemistry) are interdependent. An additional, often neglected parameter is the solvent. During high temperature nanocrystal synthesis, certain popular solvents decompose or polymerize, forming products that compromise the purity of the final NCs.[27,28] Moreover, the purity of the ligand can considerably influence the solubility of the starting precursors and provide a better capping of the final NCs.[29]

While metal, metal chalcogenide and metal halide NCs are well studied, the metal pnictides have received less attention, with the exception of metal phosphides.[9,30–33] Metal nitrides in particular are a versatile class of nanomaterials but their synthesis is not well developed. One difficulty is the higher thermodynamic stability of the oxides, compared to the nitrides (see Table 1). One can rationalize the lower standard formation free energy for nitrides because of the high bond enthalpy of dinitrogen (941 kJ mol^{-1}) *versus* dioxygen (500 kJ mol^{-1}).[34,35] Another factor is the lower ionic character of metal nitrides since the enthalpy of formation of N^{3-} is much higher than for O^{2-} (2300 kJ mol^{-1} *versus* 700 kJ mol^{-1}).[36] Only AlN and alkali(ne earth) metal nitrides are regarded as saline nitrides and they react quickly with water, releasing ammonia.[37] On the other hand, boron and silicon nitride are almost purely covalent compounds with high stability.[37] Transition metals like titanium form interstitial nitrides with extremely high chemical, thermal and mechanical stability.[37] TiN has the fcc structure of metallic titanium with interstitial nitrogen atoms in the octahedral holes (Fig. 1). Given the above considerations, it is no surprise that metal nitride synthesis is generally carried out at a high temperature and with nitrogen precursors that are more reactive than molecular nitrogen.

Here, we review the existing synthetic strategies that lead to metal nitride NCs, with a focus on the chemical conversion reactions. A broader review on nitride nanomaterials, including porous and 2D materials can be found elsewhere.[39] We target predominantly wet chemical syntheses and colloidally stable nanocrystal products. Other methods such as gas phase or solid state synthesis are only included when informative. We do not discuss nitride NCs of the alkali metals or alkaline earth metals since there are no synthetic procedures for nanocrystals available and they are extremely sensitive towards humidity, rendering them less technologically interesting. We will go systematically through the periodic system and discuss the nitrides per group, starting with group 4 and ending with group 13.

Table 1 Standard free energies of formation (kJ mol^{-1}) for selected oxides and nitrides at room temperature[38]

Oxides	$\Delta G_{\mathrm{f}}^{\circ}$	Nitrides	$\Delta G_{\mathrm{f}}^{\circ}$
TiO_2	−891.2	TiN	−309.2
ZrO_2	−1042	ZrN	−336.8
MnO_2	−464.4	Mn_3N_2	−146.4
Fe_2O_3	−744.8	Fe_2N	+12.6
CoO	−213.8	Co_3N	+8.4
CuO	−128.4	Cu_3N	+74.5
ZnO_2	−318.4	Zn_3N_2	−20.9

2. Group 4 metal nitrides

Group 4 transition metal nitrides have a high melting point, a high chemical stability and excellent corrosion resistance. TiN, ZrN and HfN have a cubic crystal structure ($Fm\bar{3}m$ space group) with a lattice constant of 4.239 Å, 4.585 Å, and 4.510 Å respectively, see Fig. 1. Their NCs exhibit a localized surface plasmon resonance (LSPR) in the visible region (HfN and ZrN) or in the near infrared regime (TiN), see Fig. 1.[40] The plasmonic response translates in a highly efficient conversion of sunlight into heat, an effect that has been used for water evaporation and desalination.[41–44] The position of the LSPR of TiN in the infrared region makes it suitable for photothermal therapies or plasmon-induced photocatalysis.[45] Given the optical properties of the group 4 metal nitrides, they are an attractive alternative for gold NCs. Furthermore, they exhibit interesting catalytic properties. ZrN NCs possess excellent activity and long-term stability (superior to platinum) as catalysts for the electrochemical oxygen reduction reaction (ORR).[46] Also HfN NPs are catalytically active for the oxygen evolution reaction (OER).[47]

Fig. 1 (a) Crystal structure of group 4 metal nitride. The metal is represented in purple and the nitrogen atom in grey. Structures plotted using VESTA.[48] Cif file obtained from ref. 49–51 (b) Absorption spectra of aqueous dispersions of TiN, ZrN, and HfN NCs. The inset shows a photograph of the NCs dispersed in water. Reprinted from ref. 40 with permission from John Wiley and Sons, Copyright 2019.

In 1988, TiN films were prepared using atomic layer epitaxy at 500 °C; $TiCl_4$ precursor was pulsed into a reactor with gaseous ammonia.[52] The colour depends on the stoichiometry of the film. For 40% N a golden yellow color is observed while for 50% a dark violet is obtained. Alternatively, $Ti(NMe_2)_4$ is reacted with ammonia. Similar strategies apply to ZrN and HfN. An extensive account of customized precursors for Chemical Vapour Deposition (CVD) of the group 4 nitrides is reviewed elsewhere.[53]

2.1. Non-thermal plasma synthesis

In 2017, powders of TiN were synthesized in a non-thermal plasma reactor (Fig. 2) from gaseous $TiCl_4$ and ammonia.[54]

$$6TiCl_4 + 8NH_3 \rightarrow 6TiN + N_2 + 24HCl \qquad (1)$$

The particle size is tuned from 3 to 8 nm by decreasing the flow rate of ammonia. The smaller particles are more oxidized than the bigger particles, but all show a plasmon resonance between 800 and 1000 nm. One can obtain ZrN nanocrystals in a similar fashion using $ZrCl_4$ and NH_3 as the precursors.[56] After synthesis, the powders need to be heated at 200 °C in an Ar atmosphere to remove the ammonium salt by-products. To avoid this last step, $TiCl_4$ was later replaced with tetrakis(dimethylamido) titanium $(Ti(NMe_2)_4)$.[55]

$$6Ti(NMe_2)_4 + 8NH_3 \rightarrow 6TiN + N_2 + 24HNMe_2 \qquad (2)$$

Also here, the particles are 6–8 nm in size (Fig. 3) and have a well-defined plasmon resonance (around 800 nm). However, the particles are not monocrystalline (consisting of 2–3 nm crystallites) and contain a considerable amount of carbon.
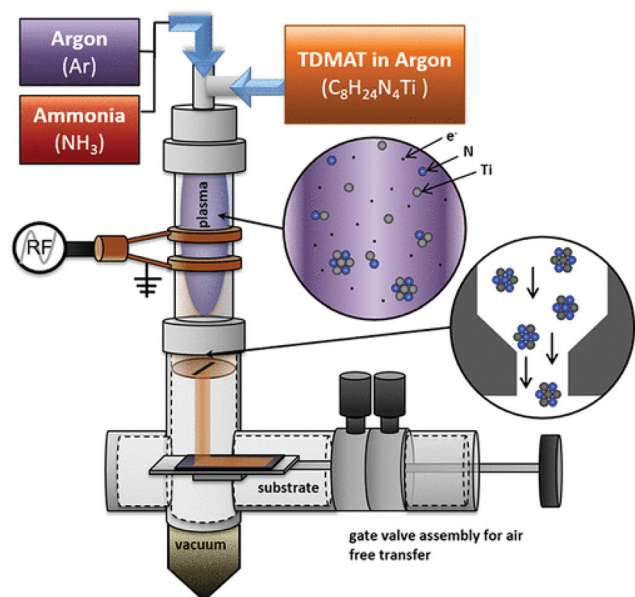

Fig. 3 High-angle annular dark-field scanning transmission electron microscopy (HAADF-STEM) images of the obtained TiN NCs via non-thermal plasma synthesis. Scale bars are (a) 20 nm and (b) 5 nm. Reprinted with permission from ref. 55. Copyright 2018 American Chemical Society.

2.2. Solution chemistry of titanium amido and imido complexes

In solution, $TiCl_4$ reacts with tert-butylamine to the mixed chloro amido complex **1**, see Fig. 4.[57] **1** has been used as a single source precursor for the CVD deposition of TiN. When **1** is reacted with triphenylphosphine oxide, **2** is formed (Fig. 4), which does not convert to TiN during CVD. Complex **1** is unstable at room temperature and slowly looses tert-butylamine, probably forming an imido species. This is supported by the formation of the monomeric tert-butylimido complex **3** by the addition of tert-butylpyridine as neutral Lewis base (Fig. 4).[58]

When $Ti(NMe_2)_4$ is treated with primary amines such as n-propylamine, n-octylamine or tert-butylamine, transamination occurs.[59–61] Subsequently, the primary amido group self-condenses and thus forms alkylimido bridges, see Fig. 5. The rate of transamination and condensation is clearly dependent on the steric hindrance between the alkyl groups of the amine

Fig. 4 Reactions of titanium chloride with tertbutylamine and thiphenylphosphine oxide or tertbutylpyridine.

Fig. 5 Transamination followed by self-condensation of primary metal amide group.

Fig. 2 Diagram of the nonthermal plasma apparatus for TiN NCs synthesis. Reprinted with permission from ref. 55. Copyright 2018 American Chemical Society.
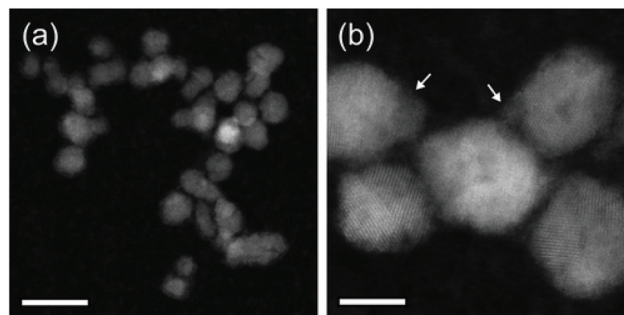
since it proceeds swiftly at room temperature for *n*-propyla-mine while *tert*-butylamine only forms the condensed product at 100 °C.[61] When using an excess of primary amine, a poly-meric, insoluble product is obtained.[60] However, sols can be formed in tetrahydrofuran (THF) by controlling the amine to titanium stoichiometry. These sols were then used to coat silica *via* dip-coating and Ti(C,N) and TiN were obtained upon pyrolysis at high temperature (minimum 800 °C) under nitro-gen or ammonia atmosphere respectively.[62]

Upon addition of one equivalent of primary amine to Ti (NMe$_2$)$_4$, the dimer **4** is formed, which can rearrange to a monomeric imido species by coordination of a Lewis base. Addition of two equivalents of trimethylsilylchloride to the latter complex yields the dichloroimido complex.[61,63] The same product can be made by the addition of a primary amine to Ti(NMe$_2$)$_2$Cl$_2$.[64] Although most of the above titanium com-plexes have not been used so far to synthesize TiN NCs, they serve as valuable inspiration for future synthetic development and grant insight in the precursors chemistry of titanium and the rest of the group 4.

Recently, titanium chloride was reacted with potassium amide in pyridine at 300 °C.[65] While the TEM image showed an isolated TiN nanocrystal of 5 nm, the XRD pattern was too broad to be consistent with a large ensemble of 5 nm crystals. Indeed, another TEM image clearly shows aggregated particles in an amorphous matrix.

2.3. Synthesis of group 4 nitride powders from the group 4 oxides

TiN NCs were obtained by Fischer *et al.* by using a mesoporous graphitic carbon nitride (mpg-C$_3$N$_4$) as both the confinement and nitrogen source.[66] In this strategy, amorphous TiO$_2$ (con-fined in the pores) is first prepared *via* a sol–gel procedure starting from TiCl$_4$ in ethanol. In a second step, this compo-site product is heated to 800 °C under inert atmosphere or in sealed quartz ampoules. The confined metal oxide is trans-formed into pure TiN while the mpg-C$_3$N$_4$ is decomposed, see Fig. 6. The size of the final TiN NCs can be slightly adjusted (5.6 nm to 7.1 nm) by controlling either the pores of the start-ing mpg-C$_3$N$_4$ or changing the concentration of the initial TiCl$_4$ precursor (filling rate). However, the resulting NCs are strongly aggregated.[66]

In 2007, Buha *et al.* investigated the thermal transform-ation of pre-synthesized anatase TiO$_2$ NCs into nanocrystalline TiN by using cyanamide or urea as a nitrogen source at 800 °C under nitrogen atmosphere.[67] Complete transform-ation is achieved when starting from 5 nm titania while with 10 and 20 nm titania, anatase impurities are still present. This reflects the solid state nature of the approach. When using a high excess of cyanamide or urea, a large amount of amorphous carbon is also produced (20–25 wt%). This can be minimized to 2 wt% by reducing the cyanamide or urea amount. The resulting TiN NCs have an average crystallite size of 3 nm and are aggregated to 50 nm agglomerates, embedded in amorphous carbon. Similarly, ZrN nanocrystals were synthesized by reacting 10–15 nm ZrO$_2$ nanocrystals with

Fig. 6 Temperature-dependent powder XRD analysis of the TiO$_2$ pre-cursor/mpg-C$_3$N$_4$ composites. (+) represents mpg-C$_3$N$_4$; (o), TiO$_2$; and (*), TiN. Reprinted from ref. 66 with permission from John Wiley and Sons, Copyright 2007.

urea at 1100 °C under an ammonia flow.[68] In 2009, Antonietti and coworkers presented the "urea glass route" which is a combination of sol–gel chemistry and the above strategy of Buha *et al.*[69] First, TiCl$_4$ is dissolved in ethanol, forming tita-nium ethoxide and releasing HCl as side product. Then a varying amount of solid urea is added to the solution and stirred until complete dissolution and the solvent is allowed to evaporate. The metal center is mostly coordinated to urea *via* the carbonyl oxygen as shown by FTIR data. The gel was then heated under N$_2$ flow at 800 °C for 3 hours at a very slow rate of 3 °C min^{-1}. A mechanism has been proposed based on thermal gravimetric analysis (TGA) and powder X-ray diffrac-tion (XRD analysis. First, a glassy intermediate with nanoscale anatase and rutile titania is formed at 400 °C. Second, at 600 °C, loss of oxygen and metal reduction/nitridation is observed. Higher temperatures (800 °C) are required to obtain a complete recrystallization, see Fig. 7. A key parameter R has

Fig. 7 XRD pattern of titanium−urea gels (R = 10) treated at different temperatures. The * symbol refers to crystalline TiO$_2$. Reprinted with permission from ref. 69. Copyright 2009 American Chemical Society.

been defined as the ratio of urea and titanium. For $R = 3$, a mixture of TiN and TiO$_2$ is obtained. Pure TiN is retrieved for $R = 4$, while Ti(C,N) was formed for $R = 10$. The higher R, the higher the carbon contamination so the optimal ratio for TiN is four. The authors expanded the procedure to many other metal nitrides (VN, NbN, GaN, CrN, Mo$_2$N), but each metal has another optimal value for R.[69] Later, the method was also applied to produce Sn$_3$N$_4$,[70] HfN,[47] and ZrN,[46] as well as other nanocomposites such as graphene g-C$_3$N$_4$ doped with TiN.[71,72] The nitride NCs obtained via this process are typically aggregated powders. Finally, other nitrogen sources were explored such as guanidine carbonate and barbituric acid. However, both features a particularly low solubility and it was not possible to achieve $R > 1$.[69]

In 2019, Karaballi and coworkers also synthesized TiN, ZrN and HfN NCs from their parent oxide NPs.[40] Their strategy consists of a high temperature (1000 °C) solid-state metathesis reaction of magnesium nitride with commercial TiO$_2$ (17 nm), ZrO$_2$ (19 nm), and HfO$_2$ (43 nm).

$$6TiO_2 + 4Mg_3N_2 \xrightarrow[\text{Ar flow}]{1000^\circ C, 1\,h} 6TiN + 12MgO + N_2 \qquad (3)$$

The final product is treated with 1 M HCl to remove MgO and unreacted Mg$_3$N$_2$, and could be dispersed in water.[40] All compounds have the expected cubic crystal structure and the nanocrystal size is 12, 15 and 11 nm for TiN, ZrN and HfN respectively. The NCs seem aggregated on transmission electron microscopy (TEM) but it is unclear whether this occurred during the sample preparation or already in solution. The reaction could be easily scaled to 1 g of metal nitride. Efforts to significantly increase the particle size by using larger oxide NCs were unsuccessful, indicating new nucleation events of the nitride, rather than a simply anion exchange reaction. The localized surface plasmon resonance of the NCs is blue-shifted and more narrow in the series: TiN, ZrN and HfN (Fig. 1). Finally, all particles were slightly oxidized at the surface and this effect was worse for ZrN and HfN, compared to TiN. This scalable strategy of Karaballi et al. appears to produce high quality group 4 nitrides. While they are highly crystalline, their size dispersion could be improved. The method has already been adopted by other groups to produce, e.g., plasmonic HfN nanocrystals.[73]

In 2017, Kan et al. explored molten salts (here: a eutectic mixture of MgCl$_2$ and NaCl) as a reaction medium for the synthesis of TiN from TiO$_2$ and Mg powder under N$_2$ atmosphere. The use of a higher Mg equivalent versus TiO$_2$ (up to 4 equivalent), higher heating temperature (up to 1100 °C), or longer reaction time (up to 7 h) leads to phase pure TiN with a better crystallinity as judged by the well-defined diffraction peaks obtained by XRD. The authors obtained 5–30 nm aggregated TiN NPs by using 2.5 equivalent of Mg heated at 1100 °C for 3 h. The authors described the mechanism as being a dissolution–precipitation type based on the increase of the surface area from the starting TiO$_2$ (9.83 m^2 g^{-1}) to the obtained TiN (93.09 m^2 g^{-1}).[74]

3. Group 5 metal nitrides

Group 5 metal nitrides (VN, NbN and TaN) have the same crystal structure as group 4 metal nitrides; a cubic crystal structure with a $Fm\bar{3}m$ space group with a lattice constant of 4.13 Å,[75] 4.394 Å,[49] and 4.331 Å (ref. 76) respectively. These group 5 nitrides exist as well in other oxidation states with less common crystal structures (orthorhombic, tetragonal and hexagonal), e.g., Ta$_3$N$_5$, Ta$_4$N$_5$ or Ta$_5$N$_6$. Vanadium nitride has attracted interest as an active material for supercapacitors (SC) due to its high specific capacitance as well as high electrical conductivity.[77] Niobium nitrides (Nb$_2$N, Nb$_4$N$_3$, NbN, etc.) are mainly investigated as superconductors. Furthermore, nitrogen-rich niobium nitrides are good candidates for electrochemical capacitors.[78,79]

VN and NbN nanopowders were synthesized via the urea glass route (see above).[69] Agglomerated VN NCs with a crystallite size of 6 nm have been synthesized by Choi et al. via a two-step method. First, ammonolysis of VCl$_4$ forms amorphous V(NH$_2$)$_3$Cl. Second, the amorphous precursor is crystallized at 400 °C in the presence of NH$_4$Cl under an ammonia atmosphere.[80] This method is one of the main chemical methods to form VN NCs,[81] as well as NbN NCs.[82]

In 1972, Ta$_3$N$_5$ powder and thin films were obtained at 1100 K starting from ammonia and Ta$_2$O$_5$ powder or Ta thin films respectively.[83] This strategy was recently pursued to prepare Ta$_3$N$_5$ nanotubes.[84] In 1995, TaN films were made using the CVD method with tert-butylimidotris(diethylamido) tantalum as precursor at temperatures ranging from 450 °C to 650 °C.[85] Nanocrystalline TaN with a cubic phase has been synthesized via a solid combustion synthesis using K$_2$TaF$_7$, NaN$_3$, and NH$_4$F precursors under high temperatures up to 850 to 950 °C.[86]

In 2011, Ho et al. have reported three methods for the synthesis of colloidal Ta$_3$N$_5$ NCs.[87] In their first method TaCl$_5$ is dispersed in octadecene (ODE). At 310 °C, tris(trimethylsilyl) amine ((TMS)$_3$N, dissolved in trioctylphosphine) is injected and the particles are left to crystallize for 20 min at 300 °C.

$$TaCl_5 + R_3P + (TMS)_3N \xrightarrow[\text{ODE}]{300-310^\circ C} Ta_3N_5 \qquad (4)$$

The resulting NCs (23 nm, see Fig. 8A) could not be redispersed in any solvent after precipitation due to a lack of strongly binding ligands. Smaller (10 nm) NCs were formed at a reaction temperature of 200 °C. The authors report that the synthesis is sensitive to the purity of TaCl$_5$; at least 99.99% purity is required, and even then the yield was very low (which was attributed to the low solubility of TaCl$_5$ in ODE). In their second method, tantalum chloride was dissolved in a mixture of oleylamine (OLAm) and trioctylphosphine oxide (TOPO). Li$_3$N was added at 300 °C.

$$TaCl_5 + Li_3N \xrightarrow[\text{TOPO, OLAm}]{300^\circ C} Ta_3N_5 \qquad (5)$$

The resulting NCs (2–8 nm after 20 min reaction, see Fig. 8B) could be redispersed in hexane after precipitation with

Fig. 8 TEM images of Ta_3N_5 obtained by Ho *et al.*[87] (a) NPs obtained with $TaCl_5$ and $(TMS)_3N$ (scale 20 nm), (b) with $Ta(NMe_2)_5$ and $(TMS)_3N$ (scale 20 nm) (c) with $TaCl_5$ and Li_3N (scale 10 nm). (d) Absorption spectrum of the obtained 10 nm Ta_3N_5. The inset showing the two limiting regimes. Adapted with permission from ref. 87. Copyright 2010 American Chemical Society.

methanol. When the reaction is left to proceed for 1 hour, 10 nm NCs are obtained. Their absorption spectrum has two absorption onsets (467 nm and 515 nm) which is explained by the absorption of Ta_3N_5 (515 nm) and that of a higher bandgap material, likely an oxidized shell. XPS data indeed confirm the presence of oxidic tantalum. To counter the low yields in the previous methods, the authors devised a third method. Pentakis(dimethylamido)tantalum and $(TMS)_3N$ were dissolved in ODE and injected in pure ODE at 300 °C (Fig. 8C). However, the formed particles were amorphous and highly sensitive to air.[87] For all three methods, the crystallinity of the resulting particles was solely assessed by TEM and an ensemble measurement (*e.g.*, XRD) is missing.

$$Ta(NMe_2)_5 + (TMS)_3N \xrightarrow[\text{ODE}]{300^\circ C} TaN_x \qquad (6)$$
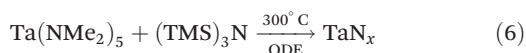
In 2013, a sol–gel pathway was demonstrated with $Ta(NMe_2)_5$ and *n*-propylamine.[88] Transamination occurs readily but the condensation appears to be slower than for titanium (see section on titanium nitride for details on transamination and condensation). Upon solvent evaporation a gel was formed. Solvent removal by vacuum resulted in a xerogel that converted in an ammonia atmosphere at 800 °C into Ta_3N_5 powder with a crystal size of 20 nm. Thin films were obtained by coating the a silica slides with the sol. Firing at 600 °C leads to TaN while heating to 800 °C yields Ta_3N_5.[88]

It is thus clear from the above that nanocrystals of the group 5 nitrides have not been convincingly obtained in colloidal form. While this is the first challenge for the future, the second challenge is to control the oxidation state and the polymorphism of these materials.

4. Nickel nitride

Nickel nitride Ni_3N has a hexagonal epsilon-Fe_3N-type structure with a $P6(3)22$ space group, see Fig. 9. The two lattice constants are 4.622 Å and 4.305 Å.[89] Nickel nitride is interesting for various applications such as lithium-ion batteries,[90] magnetic NPs,[91,92] catalysis and electrocatalysis,[93,94] including hydrogenation, hydrogen, and oxygen evolution reactions (OER).[95,96] The early chemical synthetic methods to obtain Ni_3N were based on the decomposition of nickel complexes at high temperatures and in presence of ammonia or hydrazine.[90,92]

Recently a one-step synthesis of colloidally stable Ni_3N NCs has been reported by Shanker *et al.*[97] Nickel acetate is used as precursor and OLAm is chosen as ligand. Different nanocrystal sizes are obtained (5 to 80 nm) by varying the time and temperature in a narrow window, see Fig. 10. The NCs are reasonably monodisperse and colloidally stable. The authors detect ammonia during the reaction and thus infer that ammonia is the nitrogen source. However, it is unclear how ammonia is being generated since the most logical reaction would be the formation of oleylacetamide and NiO. Furthermore, the synthesis requires a specific reagent purity and supplier.

$$Ni(CH_3CO_2)_2 + 2RNH_2 \xrightarrow[\text{ODE}]{210-230^\circ C, 5-10 \text{ min}} Ni_3N \qquad (7)$$

Fig. 9 Crystal structure of Ni_3N. The nickel atoms are represented in dark red and the nitrogen atoms in cyan and white. Structures plotted using VESTA.[48] Cif file obtained from ref. 89.
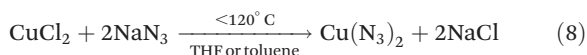

Fig. 10 TEM images of the different Ni_3N NCs obtained. (a) 5.6 ± 0.9 nm, (b) 10.6 ± 1.0 nm, (c) 36.6 ± 0.8 nm, (d) 56.4 ± 6.5 nm, and (e) 76.4 ± 3.8 nm. (f) High resolution transmission electron microscopy (HRTEM) imageof a Ni_3N nanocrystal with a size of 56.4 ± 6.5 nm. Reprinted with permission from ref. 97. Copyright 2021 American Chemical Society.

5.   Copper nitride

Copper nitride, Cu_3N, has an anti-ReO_3 crystal structure with a $Pm3m$ space group, and a lattice constant of 3.817 Å, see Fig. 11.[98,99] Copper nitride is a semiconductor with a reported band-gap of 1.7 eV which could be potentially interesting for solar cells.[100] Thin films of copper nitride have been used in optical storage devices,[101] and resistive random access memory chips.[102] Cu_3N NCs were applied as catalyst in the reduction of CO_2 to ethylene,[103] alkaline water electrolysis,[104] and the oxygen reduction reaction (ORR).[105] Cu_3N can be doped with other metals such as Pd to form Cu_3Pd_xN with $0.02 < x < 1$ which shows metallic behaviour.[106–108] The crystal structure of the latter is similar to the Cu_3N structure, with a palladium atom in the center of the unit cell (with a larger lattice constant of 3.854 Å), see Fig. 11. Cu_3N forms at relatively low temperature but decomposes at higher temperature to metallic copper. Under inert atmosphere, copper nitride films decompose at 475 °C,[101] and particles decompose at 300 °C.[109] When heated in air, Cu_3N decomposes to CuO.[109] We calculated an exciton Bohr radius of 3.12 nm for copper nitride based on the effective masses of electrons and holes, as reported by Birkett et al.[110]

In 1939, Juza et al. synthesized Cu_3N powders by reacting CuF_2 with ammonia gas (aminolyis reaction).[113] Phase pure copper nitride was obtained at reaction temperatures between 250 °C and 325 °C (6 hours reaction time).[114] At higher temperatures, Cu(0) is formed. Alternatively, Zachweija and Jacobs synthesized Cu_3N by thermal decomposition of $[Cu(NH_3)_x](NO_3)$.[111] In 2005, Choi et al. combined copper(II) chloride and sodium azide in superheated toluene or THF.[109] The intermediate copper azide decomposes to Cu_3N powder at 185 °C.

$$CuCl_2 + 2NaN_3 \xrightarrow[\text{THF or toluene}]{<120°\,C} Cu(N_3)_2 + 2NaCl \qquad (8)$$

$$6Cu(N_3)_2 \xrightarrow[\text{THF or toluene}]{185°\,C} 2Cu_3N + 17N_2 \qquad (9)$$

The reaction temperature is remarkably lower than previously reported for the similar synthesis of other metal nitrides such as TiN and GaN. Unfortunately, the reaction time is very long (about three days) and metal azides are thermally

Fig. 11 Crystal structure of Cu_3N and the doped Cu_3PdN. The copper is represented in dark red, the palladium in grey and the nitrogen atom in cyan. Structures plotted using VESTA.[48] Cif file obtained from ref. 111 and 112.

unstable and shock sensitive, which limits the reaction to small scales. Finally, the obtained Cu_3N is not phase-pure and some NaCl impurities remain present in the sample.

5.1. Cu_3N nanocrystal synthesis from copper nitrate and primary amine

In 2011, Wang et al. obtained colloidally stable Cu_3N NCs by reacting $Cu(NO_3)_2 \cdot 3H_2O$ in octadecylamine (ODA) at 220–280 °C.[115] Octadecylamine acts here both as solvent and as ligand.

$$Cu(NO_3)_2 + 32RNH_2 \xrightarrow[\text{10−60 min}]{220−280°\,C} Cu_3N \qquad (10)$$

The authors hypothesize that NO_2 and O_2 are formed as side products but did not provide experimental evidence. This hypothesis was based on the solid state decomposition reaction of $Cu(NO_3)_2 \cdot 3H_2O$ into CuO, NO_2 and O_2 at around 180 °C.[116] The size of the NCs is tuned by using different reaction temperatures (220–280 °C) and reaction times (5–20 min). The conditions and their outcomes are also summarized in Table 2. Pure Cu_3N NCs are only obtained with 32 equivalents of ODA. Cu_2O is obtained with 8 equivalents, while 80 equivalents lead to Cu(0) NCs. Forty and thirteen equivalents lead to a mixture of Cu/Cu_3N or Cu_3N/Cu_2O mixture respectively. Please note that the copper concentration also changes in these experiments since ODA is the solvent. Wang et al. argue that nitrate (NO_3^-) is the nitrogen source for the nitride (N^{3-}), even though this would involve the transfer of eight electrons to N(V) in nitrate. They based their argument on the observation that copper nitrate is the only precursor that delivers copper nitride. Copper chloride does not yield any products while copper acetate yields a $Cu(0)/Cu_2O$ mixture and copper sulfate delivers copper sulfide NCs. However, no other hypotheses were tested or disproved, thereby leaving the option open that the nitride is provided by ODA, as is the case for certain syntheses of InN NCs (see below).

Also in 2011, Wu and co-workers described the formation of Cu_3N from $Cu(NO_3)_2 \cdot 3H_2O$ in the presence of both a primary amine (surfactant) and octadecene (ODE) (solvent), see eqn (11).[117] By changing the primary amine (ODA, hexadecylamine or OLAm), the size of the final Cu_3N varies from 26 ± 5.6 nm to 18 ± 2.3 nm and 10 ± 2.7 nm respectively (Fig. 12). All NCs have a cubic morphology and are phase-pure copper nitride.

$$Cu(NO_3)_2 + 66RNH_2 \xrightarrow[\text{250° C,30 min}]{150°\,C,3\,h} Cu_3N \qquad (11)$$

In a first stage, the reaction is heated to 150 °C with a concomitant color change from dark blue to green and then yellow, indicating the reduction of Cu(II) to Cu(I).[115] Subsequently, the solution is heated to 250 °C for 30 min and the solution turns brown, consistent with the formation of copper nitride. According to Wu et al. ODE is necessary as solvent to obtain well-defined nanocubes since irregular and polydisperse Cu_3N NCs have been obtained using only OLAm. Most likely, other solvents would be more suitable since ODE polymerizes during nanocrystal synthesis.[27] Nonetheless, this

Table 2 Synthetic conditions for colloidal copper nitride NCs

Precursor[a]	[Cu] (mM)	Solvent[b]/ ligand[c]	Ligand/ Cu ratio	Temperature (°C)	Time (min)	Morphology	Phase	Size (nm)	Ref.
$Cu(NO_3)_2 \cdot 3H_2O$	101	ODA	32	240	10	Cubic	Cu_3N	15	115
$Cu(NO_3)_2 \cdot 3H_2O$	101	ODA	32	280	5	Spherical	Cu_3N	10	115
$Cu(NO_3)_2 \cdot 3H_2O$	101	ODA	32	260 + 240	5 + 5	Spherical	Cu_3N	15	115
$Cu(NO_3)_2 \cdot 3H_2O$	101	ODA	32	220 + 240	5 + 5	Spherical	Cu_3N	15	115
$Cu(NO_3)_2 \cdot 3H_2O$	101	ODA	32	220	20	Irregular	Cu_3N	50	115
$Cu(NO_3)_2 \cdot 3H_2O$		ODA	40	240	10		$Cu + Cu_3N$		115
$Cu(NO_3)_2 \cdot 3H_2O$		ODA	13	240	10		$CuO + Cu_3N$		115
$Cu(NO_3)_2 \cdot 3H_2O$	24	ODE/ODA	67	250	30	Cubic	Cu_3N	26	117
$Cu(NO_3)_2 \cdot 3H_2O$	24	ODE/HDA	69	250	30	Cubic	Cu_3N	19	117
$Cu(NO_3)_2 \cdot 3H_2O$	24	ODE/OLAm	63	250	30	Cubic	Cu_3N	11	117
$Cu(NO_3)_2 \cdot 3H_2O$	24	OLAm		250	30	Irregular	Cu_3N		117
$Cu(NO_3)_2 \cdot 3H_2O$	25	ODE/OLAm	31	240	15	Cubic	Cu_3N		118
$Cu(NO_3)_2 \cdot 3H_2O + Pd(acac)_2$	25	ODE/OLAm	31	240	15	Cubic	Cu_3PdN	16	118
$Cu(NO_3)_2 \cdot 3H_2O + Pd(acac)_2$	25	ODE/OLAm	31	190	30	Cubic	Cu_3PdN		119
$Cu(NO_3)_2 \cdot 3H_2O$	25	ODE/OLAm	31	210	30	Cubic	Cu_3N		119
$Cu(NO_3)_2 \cdot 3H_2O$	75	ODA/OLAm	45	240	20	Cubic	Cu_3N	25	105
$Cu(NO_3)_2 \cdot 3H_2O$	88	ODA/OLAm	41	240	30	Cubic	Cu_3N	25	103
$Cu(NO_3)_2 \cdot 3H_2O$	88	ODA/OLAm	41	250	30	Cubic	Cu_3N	20	103
$Cu(NO_3)_2 \cdot 3H_2O$	88	ODA/OLAm	41	260	30	Cubic	Cu_3N	10	103
$Cu(NO_3)_2 \cdot 3H_2O$	88	ODA/OLAm	41	230	30	Spherical	Cu_3N	20	103
$Cu(NO_3)_2 \cdot 5H_2O + HMT$	50	Hexanol	—	200	60	Spherical	Cu_3N	80	122
$Cu(acetate)_2 \cdot H_2O + NH_3$	10	Nonanol	—	190	60	Spherical	Cu_3N	200	123
PPC	50	ODA	74	260	5	Spherical	Cu_3N	3	124
$Cu(NO_3)_2 \cdot 3H_2O$	50	ODA	74	260	5	Cubic	Cu_3N	19	124
$Cu(OMe)_2$	92	$BnNH_2$	117	140	15	Spherical	Cu_3N	2	125
$CuI + KNH_2 + NH_3$	21	Pyridine	—	−35 + 130	10 + 30	Spherical	Cu_3N	4	126

[a] HMT = hexamethylenetetraamine, PPC = pyrrole-2-carbaldpropyliminato Cu(II). [b] ODE = 1-ODE. [c] ODA = octadecylamine, OLAm = oleylamine, HDA = hexadecylamine.

Fig. 12 TEM images and the corresponding size histograms of Cu_3N NCs synthesized from copper nitrate and various primary amines in ODE solvent, according to ref. 117. (a, b) Octadecylamine (c, d) hexadecylamine, and (e, f) oleylamine. Reprinted with permission from ref. 117. Copyright 2011 American Chemical Society. Note that the authors labelled the axis *diameter*. Given the cubic morphology of the nanocrystals, this is confusing and the cube edge length is a more appropriate measure for the size.

method was adopted by other groups and Vaughn II *et al.* used it to produce Cu_3N and Cu_3PdN, albeit with half the number of amine equivalents, see also Table 2.[118] The reaction mixture is degassed for 10 min at 120 °C and then heated to 240 °C under argon for 15 min. To produce Cu_3Pd_xN, $Pd(acac)_2$ is also added at the start. The average diameter of the quasicubic Cu_3PdN NCs is 16 ± 2 nm. Cu_3N and Cu_3PdN can also be grown on Pt and Au nanoparticle seeds to form nanoscale heterostructures at 190 °C see Fig. 13.[119]

In 2019, Braman *et al.* synthesized Au decorated Cu_3N NCs. First, Cu_3N NCs (10 ± 5 nm) were obtained *via* a similar approach to the one of Vaughn *et al.* but with a higher amine equivalent and a lower heating temperature (210 °C). Subsequently, Au NPs were grown on top of the Cu_3N cubes. The resulting heterostructure demonstrated a better catalytic activity than pure Cu_3N.[120]

In 2014, Xi *et al.* performed the reaction in a mixture of ODA and OLAm.[105] First the mixture is heated to 110 °C and than quickly heated to 240 °C for 10 min. They obtained uniform nanocubes of Cu_3N of around 20 nm. The growth mechanism was investigated by analyzing reaction aliquots at 2, 5 and 10 min. From TEM measurements (Fig. 14), Xi *et al.* conclude that first small NPs are formed, which subsequently ripen into bigger nanocubes. This growth mechanism was later confirmed under slightly different conditions.[121] In addition, long reaction times (at 260 °C) lead to the decomposition of the formed Cu_3N to Cu(0) particles. Xi *et al.* also studied the magnetic properties of the Cu_3N NCs and observed

Fig. 13 Time-dependent growth studies of Cu_3PdN on Pt nanocubes at 170 °C for (a−f) 5 min, (g−l) 10 min, and (m−r) 15 min. The data for each time point include (a, g, and m) TEM images, (b, h, and n) HAADF-STEM images, (c−e, i−k, and o−q) energy dispersive X-ray spectroscopy (STEM-EDS) element maps for Pt (red), Cu (blue), and Pd (green), and (f, l, and r) HRTEM images of individual particles. Reprinted with permission from ref. 119, Copyright 2019 American Chemical Society.

Fig. 14 (A) TEM of the Cu_3N NCs synthesized according to ref. 105, after 2, 5 and 10 min. (B) The proposed growth procedure of Cu_3N nanocubes. Reproduced from ref. 105 with permission from the Royal Society of Chemistry.

paramagnetic and ferromagnetic contributions. Such properties are not expected for d^0 materials and are assumed to originate from surface defects.[105]

In 2019, Yin *et al.* used the same strategy of Xi *et al.* By tuning the heating temperature, the size and morphology of the final Cu_3N is changed, see Table 2.[103] Above 240 °C cubic NCs are formed while below 240 °C spherical NCs are formed. The size of the final Cu_3N decreases from 25 nm to 10 nm by increasing the reaction temperature from 240 °C to 260 °C. The Cu_3N NCs are stable even after 2 weeks of air exposure and no degradation is observed in the crystal structure and morphology.

5.2. Cu_3N nanocrystal synthesis from $Cu(OMe)_2$ and benzylamine

Deshmukh *et al.* reacted $Cu(OMe)_2$ in benzylamine ($BnNH_2$) and obtained very small, spherical Cu_3N NCs (2.2 ± 0.5 nm).[125,127]

$$Cu(OMe)_2 + 117 BnNH_2 \xrightarrow[\text{15 min}]{140°C} Cu_3N \qquad (12)$$

Fig. 15 Proposed reaction mechanism of $Cu(OMe)_2$ with $BnNH_2$ that leads to the formation of Cu_3N.[125] Molecules in red are the one detected by GC-MS.

The standard synthesis is performed at 140 °C under inert atmosphere, in a pressure tube. Over the course of the reaction, the color changes from dark blue to red. The average crystal size (determined from XRD) is quite insensitive to the reaction conditions (80 °C–180 °C, 5–60 min) and varies from 1.8 to 2.8 nm. The authors further suggested a precursor conversion mechanism by analyzing the reaction by-products with gas chromatography–mass spectrometry (GC-MS), see Fig. 15. In the first step, copper(II) methoxide oxidizes $BnNH_2$ to benzenemethanimine and is reduced to Cu(I). This proposal is based on the detection of methanol in GC-MS. This reactivity is special for $Cu(OMe)_2$ since other Cu(II) salts such as Cu(II) chloride make stable complexes with amines and fail to produce Cu_3N. The benzenemethanimine intermediate reacts with benzylamine, yielding *N*-benzylidenebenzylamine (detected by GC-MS) and ammonia. The *in situ* formed ammonia reacts with Cu(OMe) to form Cu_3N. Traces of benzonitrile are also observed at the GC, which is justified by further oxidation of benzenemethanimine in presence of Cu(II). This synthetic strategy was adopted by Liu and co-workers, but also requires a specific reagent purity and supplier.[128]

5.3. Cu_3N nanocrystal synthesis *via* sol–gel chemistry

In aqueous sol–gel chemistry, dissolved metal precursors are hydrolyzed with water and further condense in metal oxide particles and gels.[129] Similarly, researchers have synthesized copper nitride NCs by aminolysis (reaction with ammonia) and condensation. In 2018, Egeberg *et al.* reacted CuI with ammonia under basic conditions to form $Cu(NH_2)_2$.[126]

$$CuI \xrightarrow[\text{pyridine}, -35°C]{KNH_2/lq\text{-}NH_3} Cu(NH_2) \xrightarrow[\text{pyridine}, 130°C]{NH_3\uparrow} Cu_3N \qquad (13)$$

By condensation of the copper amide under reflux conditions, small copper nitride NCs are obtained (4.2 ± 0.7 nm), see Fig. 16. Only pyridine is observed at the surface of the NCs according to FT-IR and elemental analysis, which could explain why these NCs are air and moisture sensitive.

Fig. 16 TEM images of Cu_3N NCs synthesized by sol–gel chemistry according to ref. 126. Reproduced from ref. 126 with permission from the Royal Society of Chemistry.

Alternatively, Nakamura *et al.* have formed Cu_3N from copper(II) acetate in nonanol by bubbling ammonia through the mixture at 190 °C for 1 h.[123] The final NCs are not colloidally stable and form aggregates of about 200 nm with crystallite sizes of 20–30 nm. The same colour changes are observed; from blue to yellow to dark brown. Single phase CuO is formed by using shorter chain alcohols such as pentanol, hexanol and heptanol at 130 °C. With increasing temperature, an increasing amount of copper nitride is obtained and from 170 °C pure copper nitride is formed. The authors propose the following mechanism. First, ammonia forms a complex with Cu(II), evidenced by a color change from green to blue. Second, the authors hypothesize Cu(II) is reduced by nonanol. The color change to yellow is consistent with a Cu(I) species but the authors do not detect the direct product, nonyl aldehyde. They do detect 9-ODEamide, of which it is unclear how it is exactly formed. Finally, the Cu(I) species reacts with ammonia to form copper nitride. In the background, there is also the esterification of acetate with nonanol to nonyl acetate. According to the mechanism, a lot of protons are released but the authors did not try to uncover the fate of these protons. Nor were alternative hypotheses considered such as the reduction of Cu(II) by ammonia itself.

5.4. Alternative precursors for Cu_3N nanocrystal synthesis

In 2018, Mondal and co-workers obtained Cu_3N by reacting hexamethylenetetraamine (HMT) and $Cu(NO_3)_2 \cdot 5H_2O$ in *n*-hexanol at 200 °C for one hour under an inert atmosphere.[122] HMT undergoes hydrolysis and forms formaldehyde and NH_3. The latter is the source of nitrogen as described in Fig. 17. Copper nitrate is in this case simply the source of water and Cu and not the nitrogen source. Cu(II) is assumed to be reduced by the formaldehyde intermediate, but the authors do not show evidence for the formation of formic acid. The final NCs are around 80 nm in size, which is most likely due to the absence of a strongly coordinating ligand.

Also in 2018, Sithole *et al.* synthesized a novel copper precursor: pyrrole-2-carbaldpropyliminato Cu(II) (PPC), see Fig. 18.[124] PPC is synthesized from pyrrole-2-carboxaldehyde, copper acetate and propylamine in deionized water, filtered

Fig. 17 Proposed reaction mechanism for Cu_3N formation from hexamethylenetetraamine and $Cu(NO_3)_2 \cdot 5H_2O$.[122]

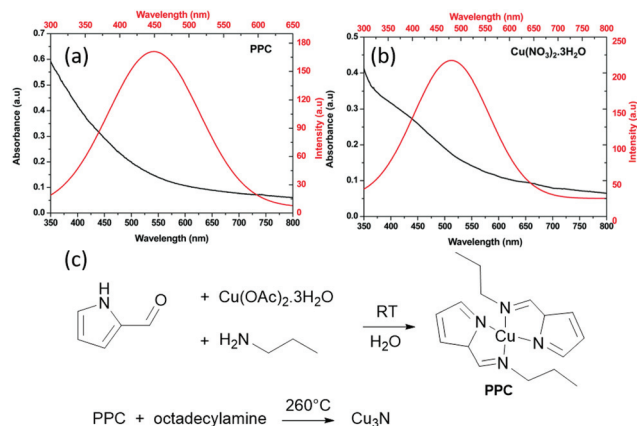**Fig. 18** UV-Vis absorption and photoluminescence spectra of Cu_3N obtained *via* (a) PPC and (b) $Cu(NO_3)_2 \cdot 3H_2O$ method. Reprinted from ref. 124 with permission from the Royal Society of Chemistry. (c) Reaction mechanism proposed for Cu_3N formation from the reaction of pyrrole-2-carbaldpropyliminato Cu(II) (PPC) and ODA shown below.[124]

and recrystallized. In a second step, PPC is heated with ODA to form Cu_3N (Fig. 18). The resulting spherical NCs are about 1.5–4 nm in diameter, in contrast to the 18 nm cubes that are obtained with copper nitrate under identical conditions. The photoluminescence of the smaller Cu_3N NCs is slightly blue-shifted to the emission of the larger NCs, which could possibly be ascribed to quantum confinement. Indeed, we estimated from the calculated dielectric constant and the effective hole and electron masses, an exciton Bohr radius of about 3 nm. However, a direct relation between size and optical properties is currently missing.

6. Zinc nitride

Zn_3N_2 has a cubic crystal structure ($Ia\bar{3}$ space group) with a lattice constant of 9.7691 Å (Fig. 19).[130] It is a nontoxic, earth-abundant, and low-cost semiconductor,[131] and is therefore promising for various applications. However, it has been less exploited than other nitrides due to the difficulties in preparation and its high reactivity towards water.[132] As a II–V semiconductor, Zn_3N_2 has a high electron mobility and carrier concentration. The reported band gap for Zn_3N_2

Fig. 19 (a) Crystal structure of Zn_3N_2 metal nitride. The metal is represented in purple and the nitrogen atom in grey. Structures plotted using VESTA.[48] Cif file obtained from ref. 130. (b) Toluene solutions of OLAm capped Zn_3N_2 NCs sampled at different reaction times and excited with a 365 nm lamp. (c) Absorption (thin lines) and emission (thick lines) spectra of Zn_3N_2 NCs with mean diameters of 2.1 ± 0.4 nm (solid lines), 4.6 ± 2.3 nm (dashed lines) and 7.1 ± 2.0 nm (dotted lines). Reproduced from ref. 136 with permission from the Royal Society of Chemistry.

varies from 1.0 to 3.3 eV depending on the preparation methods.[133–135]

Various physical methods or nitridation approaches have been employed to synthesize Zn_3N_2 as thin films,[137] powders,[138] hollow balls,[139] or nanowires.[134] One chemical approach was reported by Taylor *et al.* where diethylzinc was reacted with an ammonia flow in ODE, with OLAm as the capping ligand.

$$ZnEt_2 + NH_3 \xrightarrow[\text{ODE, OLAm}]{225^\circ C} Zn_3N_2 \qquad (14)$$
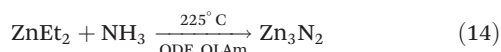
The size is tuned by the stepwise addition of the diethylzinc precursor. Thus, NCs emitting in the range 500–1100 nm were obtained,[140] with a photoluminescence quantum yield greater than 50%. The authors further investigated the effect of the ratio between the diethylzinc to ammonia on the growth. A lower ammonia flow rate or higher diethylzinc injection promotes growth and large particles are obtained. Higher ammonia flow rates lead to smaller NCs.[136]

7.   Group 13 nitrides

Among the group 13 nitrides, GaN has acquired most fame due to its use in blue LEDs, a feat that has been awarded with the 2014 nobel prize in Physics.[141] The most stable phase of the group 13 nitrides has the wurtzite crystal structure. The bandgap of AlN, GaN and InN is 6.2 eV, 3.4 eV and 0.7 eV respectively. As discussed before AlN is the least interesting nitride of group 13 since it is considered a saline nitride and quickly reacts with water. However, aluminum nitride (AlN) has a high thermal conductivity (up to 320 W m^{-1} K^{-1}), high acoustic wave velocity, and electrical resistance.[142] These properties raise the potential of AlN for applications such as thermal interfaces for electronic laser, brackets for LED technology, resonators, sensors, actuators, *etc.*[143–145] The different synthetic approaches for cubic AlN formation have been presented elsewhere.[146]

GaN and InN nanocrystals are considered the possible next generation of QDs. While the exciton Bohr radius of gallium nitride is 3.2 nm, the exciton Bohr radius of indium nitride is 8 nm. Together with the formation of solid solutions ($In_xGa_{1-x}N$), this provides ample opportunity to tune the optical properties using either quantum confinement or compositional control. GaN is being investigated for high frequency and high power transistor design.[147,148] InN is a promising compound for optoelectronic applications due to its low bandgap, small effective mass and efficient electron transport. InN is also considered for low-cost, high-efficiency solar cells, photomasks, laser diodes, sensors, and biological imaging.[149–153] InN has a complex plasmonic behavior due to a nonparabolic dispersion of its conduction band.[154,155]

7.1.   Synthesis of group 13 nitride powders

In 2004, InN was prepared by the conversion of In_2O_3 under ammonia flow in a temperature range of 600 °C to 730 °C. Depending on the temperature, either spherical NCs or hollow microtubes are formed. This is due to the decomposition of InN at a temperature around 650 °C into metallic In and nitrogen[156]

$$In_2O_3 + 2NH_3 \rightarrow 2InN + 3H_2O$$

$$2InN \xrightarrow{650^\circ C} 2In + N_2$$

GaN NCs in a silica matrix were synthesized by first forming an oxide gel of gallium and silicon. The gel is then annealed at 900 °C for 5 h under NH$_3$ atmosphere.[157] Variations on this strategy exist where pure GaN nanocrystalline powders are formed by annealing Ga_2O_3, GaO(OH), or NH$_4$[Ga(OH)$_2$CO$_3$] under an NH$_3$ atmosphere at 900–950 °C.[158–161] Similar to the case of TiN, the solid state reaction between Ga_2O_3 (or γ-Al$_2O_3$) and cyanamide CN_2H_2

yields GaN (or AlN) NCs.[67,162] Finally, the urea glass route was also successful in synthesizing GaN nanopowders.

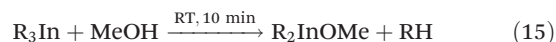### 7.2. Synthesis strategies based on azide or amide precursors

Colloidally stable, but poorly crystalline GaN NCs are obtained by refluxing $[Et_2Ga(N_3)]_3$, $(N_3)_2Ga[(CH_2)_3NMe_2]$, or $(Et_3N)Ga(N_3)_3$ in triglyme at 220 °C for 5 hours.[163] Also, $GaCl_3$ and NaN_3 react to form gallium azide, which forms amorphous GaN at 220 °C or 260 °C in THF or toluene respectively. Annealing and NaCl removal are necessary in order to form crystalline powders.[164] Finally, crystalline GaN NCs were formed from NaN_3 and metal Ga by heating to 700 °C under nitrogen in a high-pressure apparatus.[165]

Janik et al. formed GaN NCs via pyrolysis at 450–500 °C of a gallium imide $[Ga(NH)_{3/2}]_n$ precursor (obtained by reaction of $[Ga(NMe_2)_3]2$ and NH_3).[166] In 1999, this method was improved by crystallizing the $[Ga(NH)_{3/2}]_n$ precursor in hot trioctylamine (360 °C for 24 h) under a flow of ammonia.[167] During cool-down of the reaction mixture, a solution of hexadecylamine in trioctylamine was added, which improved the colloidal stability of the final GaN NCs. These NCs have a diameter of 3 nm and feature a first exitonic emission at 3.65 eV, higher than the bulk bandgap of GaN.

β-GaN NPs of 3–8 nm in size were obtained via microwave heating of $Ga(NH_2)_3$ in ionic liquid at 300 °C for 1 h. The colorless suspension of $Ga(NH_2)_3$ was obtained by dissolving $GaCl_3$ in liquid NH_3 at −35 °C and adding KNH_2. The obtained NCs show a bandgap around 3.9 eV which is 0.6 eV above the β-GaN bulk bandgap. The authors attributed this blue shift to quantum confinement. The fluorescence properties of the as-synthesized NCs are shown in Fig. 20.[168]

In 2006 Dingman et al. reported the synthesis of InN nanofibres at low temperatures (203 °C), catalyzed by nanometer sized droplets of In metal (also called a solution–liquid–solid (SLS) mechanism).[169] The authors prepared two different indium precursors ($^iPr_2InN_3$ and $^tBu_2InN_3$) by reacting trialkyl-indium first with methanol and subsequently with trimethyl-silylazide. Crystalline InN was then formed by reacting the as mentioned precursors with 1,1-dimethylhydrazine (H_2NNMe_2) at 203 °C for 20 h. The role of 1,1-dimethylhydrazine is to reduce part of the indium precursors to In droplets, which then catalyze the InN crystallization.

$$R_3In + MeOH \xrightarrow{RT, 10\,min} R_2InOMe + RH \quad (15)$$

$$R_2InOMe + TMSN_3 \xrightarrow{RT, 210\,h} R_2InN_3 + TMSOMe \quad (16)$$

$$R_2InN_3 + H_2NNMe_2 \xrightarrow[20\,h]{203°C} InN \quad (17)$$

In 2006 Choi et al. synthesized InN NCs from indium bromide and sodium azide under solvothermal conditions.[170] The indium azide intermediate decomposes into InN and N_2.

$$InBr_3 + 3NaN_3 \xrightarrow{280°C} [In(N_3)_3] + 3NaBr \quad (18)$$

$$[In(N_3)_3] \xrightarrow{280°C} InN + 4N_2 \quad (19)$$
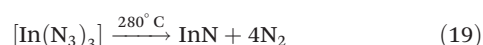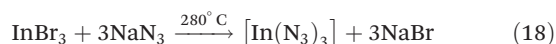
The solvent used during the solvothermal treatment determines the final properties of the NCs. While toluene delivered 10 nm aggregated wurtzite InN, hexadecane yielded poorly crystalline InN. The reaction typically takes 3–5 days during which the reaction temperature was increased step by step to avoid explosive azide decomposition. Also $In_xGa_{1-x}N$ alloyed particles were synthesized via this strategy.[170]

The reaction of potassium amide (KNH_2) and indium iodide in liquid ammonia yields an insoluble indium amide product. The latter is probably highly condensed, featuring imido bridges. Decomposition of this insoluble product at 400 °C under nitrogen atmosphere delivers InN, In, KNH_2, and NH_3.[171] Alternatively, InI_3 and $NaNH_2$ were reacted in anhydrous benzene in a Teflon-lined pressure bomb.[172] The crystallite size of the resulting InN NCs varies from 9.9 ± 5 nm to 35.1 ± 10 nm by increasing the reaction time or temperature. At ambient pressure, InN NCs (6.2 ± 2 nm diameter) have been synthesized using $InBr_3$ and $NaNH_2$ in hexadecane under an ammonia atmosphere.

$$InBr_3 + 3NaNH_2 \xrightarrow[3\,h]{250°C} InN + In \quad (20)$$

A post-synthetic acid treatment (to remove In(0)) and functionalization with OLAm yielded colloidally stable particles, see Fig. 21.[173] This method has been further studied by Palomaki et al. where they use In_2S_3 instead of $InBr_3$ and ODE as their solvent.[174]

$$In_2S_3 + NaNH_2 \xrightarrow[15\,min - 12\,h]{175-220°C} InN + In \quad (21)$$

To improve the size dispersion, size-selective precipitation was performed by the dropwise addition of acetonitrile to OLAm-capped InN NCs, and centrifugation. The final nanocrystal size was tuned from 4.5 to 9.9 nm by varying the reaction time from 15 min to 12 h at 220 °C. The NCs size also increases from 4.1 to 8.0 nm by increasing the reaction temperature from 175 °C to 200 °C (at a fixed reaction time of three hours). Below 175 °C no InN was formed.

When $InCl_3·4H_2O$, $NaNH_2$, and sulfur were reacted in a pressure bomb at 160 °C for 30 h, wurtzite InN crystals

Fig. 20 (a) Emission spectrum at 274 nm and excitation spectrum at 523 nm of the synthesized GaN. (b) Photographs of the as synthesized GaN NCs in daylight and under excitation at 254 nm. Reprinted from ref. 168 with permission from the Royal Society of Chemistry.

Fig. 21 TEM images of the colloidally stable InN obtained by Hsieh *et al.* after acid treatment. (a) Low magnification image, (b) high resolution image and (c) diffraction pattern obtained *via* fast Fourier transform (FFT). Reprinted with permission from ref. 173 with permission from the Royal Society of Chemistry.

Fig. 22 TEM images of the NPs. (a) Overview of the as prepared sample, showing the InN branches stemming out of larger In(0) NPs. (b) HRTEM image of one of the InN branches in (a) at the surface of the In (0) nanoparticle. XRD pattern for the (c) as-prepared sample and (d) acid treated sample. The vertical lines show the XRD patterns of bulk zinc blende-InN (red) and tetragonal In(0) (blue). Reprinted with permission from ref. 176. Copyright 2016 American Chemical Society.

(50–200 nm) were obtained.[175] According to XRD, the reaction proceeds through a In_2S_3 intermediate. Even larger particles (500 nm) were obtained using $In(NO_3)_3 \cdot 5H_2O$ as precursor.

7.3. Colloidal InN NCs from lithium oleylamide

Karan and coworked reported a surfactant-assisted procedure where all precursors are soluble.[176] $InBr_3$ is first dissolved in a mixture of OLAm and ODE solvent (or hexadecane). At 220 °C the authors inject lithium oleylamide, which was synthesized from OLAm, *n*-butyllithium (*n*-BuLi) and tetramethylethylenediamine (TMEDA). After 10 minutes, the reaction is stopped and the product is purified. TEM analyis shows that the obtained particles consist of a 30 nm In(0) core and InN outgrowths (Fig. 22). The mixed composition of In and InN is confirmed by XRD with sharp reflections for In and broader reflections for InN, consistent with their size difference (Fig. 22). Using the same strategy as mentioned before, In is removed by an nitric acid treatment and the InN NCs are stabilized by functionalization with OLAm.[176]

Intrigued by the high dissociation energy of C–N bonds (330 kJ mol^{-1}), Beaulac *et al.* investigated the mechanism of this reaction by analyzing the by-products *via* ^{1}H NMR, ^{13}C NMR, 2D COSY NMR, and mass spectrometry.[177] The authors propose that oleylamide is oxidized to oleylimine, thereby reducing In(III) to In(0), see Fig. 23. A second equivalent of oleylamide performs a nucleophilic attack on the imine, yielding a secondary aldimine and releasing NH_2^-. The latter goes on to react with In(III) to form InN. The proposed mechanism is based on the observation of secondary aldimine, ammonia,

Fig. 23 Overall reaction. Reaction 1a, alkylamide precursor oxidation; reaction 1b, formation of the secondary imine leading to NH_2^- production; reaction 2, nitride formation; R1, R2, R3, three hypothetical reduction processes concomitant with reaction 1a; S1, detrimental hypothetical side reaction. Orange, reactants; blue, intermediates (not isolated); red, identified products. Uncoordinated forms depicted here for simplicity. Reprinted with permission from ref. 177. Copyright 2018 American Chemical Society.

hydrogen, InN and In as reaction products. Oleylimine is too unstable to be isolated. In(0) is always formed in larger yields than InN, meaning that not all reactive NH_2^- are converted to InN.

7.4. Other surfactant based strategies for colloidal nitrides

$AlCl_3$, $GaCl_3$, and $InCl_3$ react with urea to form the crystalline complexes: $[Al(H_2NCONH_2)_6]Cl_3$, $[Ga(H_2NCONH_2)_6]Cl_3$, and $[In(H_2NCONH_2)_3Cl_3]$.[178] In the Al and Ga complexes, six urea

molecules are coordinated to the metal and the chloride is simply the counter ion of the positively charged complex. In the In complex, three urea molecules and 3 chlorides build up the first coordination sphere. Pyrolysis of the complexes under nitrogen yields AlN, GaN or a mixture of InN and In_2O_3. Refluxing $[Ga(H_2NCONH_2)_6]Cl_3$ in trioctylamine (365 °C) for 24 hours yields colloidal GaN NCs (2–3 nm). These particles show photoluminescence (PL) emission bands at 340 and 380 nm. Refluxing the Al and In complex yields AlN and InN (with a minor indium oxide impurity) respectively. Later, the authors showed that the obtained GaN NCs were amorphous and further annealing in ammonia at 450 °C for 24 h was necessary to improve their crystallinity.[179]

In 2019, Chang Choi et al. designed a hot-injection strategy to obtain GaN QDs.[180] Gallium chloride and stearic acid were dissolved in ODE and heated to 280 °C under argon. Subsequently, a solution of lithium bis(trimethylsilyl)amide in hexane was rapidly injected.

$$GaCl_3 + LiN(TMS)_2 \xrightarrow[\text{ODE, stearic acid}]{220-280^\circ C, 10-90 \text{ min}} GaN \qquad (22)$$

The nanocrystal size was hard to determine from TEM but surely below 5 nm, which is also confirmed by the very broad nature of the XRD reflections. The PL emission of the QDs could be tuned from 315–355 nm, while the bulk PL is at 365 nm. Successful doping with zinc red-shifted the PL to 330–460 nm.[180]

8.   Summary and outlook

We have focused on precursor chemistry that allows synthesizing colloidal metal nitrides varying from plasmonic nitrides (Group 4) to semiconductors (Group 13). Approaches that lead to nanocrystal formation are described based on a systematic comparison between synthetic strategies. To date, the late transition metal and group 13 metal nitrides have been more extensively studied. While the reaction mechanism (precursor conversion) is most studied for the group 13 nitrides, the most uniform nanocrystals are obtained for Cu_3N. At the same time, we were forced to conclude that there does not exist any convincing reports of a colloidal synthesis of group 4 and group 5 nitrides. Only nanopowders were succesfully obtained, of which some could be dispersed in water, albeit in aggregated form. It is striking that the ease of nitride formation seems to correlate with the valence of the elements. Whereas Cu^+ and Ni^+ easily crystallize as nitrides, Ga^{3+} and In^{3+} are more difficult to crystallize and the most successful approaches are based on crystallization, catalyzed by liquid nanodroplets of metal. An additional hurdle for the group 4 and 5 nitrides is the required reduction during the synthesis. For example, most common precursors for TiN and TaN are based on Ti(IV) or Ta(V), while the final nitrides contain the metal in the +III oxidation state. To avoid the reduction step, future precursors of group 4 and 5 nitrides could start from the metal in the correct oxidation state. When designing new precursors, it is

also useful to keep in mind the lessons from the metal chalcogenide field. The consensus seems to be that for optimal nanocrystal formation (and control over size), the conversion of precursor (P) to monomer (M) needs to be slow, relative to the crystallization (nucleation and growth) of the monomer into the final nanocrystals.

$$P \xrightarrow{\text{slow}} M \xrightarrow{\text{fast}} NC \qquad (23)$$

Since group 4 and 5 nitrides typically require high temperatures for crystallization, the logical conclusion is that their crystallization rate is low. Therefore, one should design nitride precursors that decompose even slower, or to apply strategies that enhance the rate of crystallization by lowering the barrier for bond forming and bond breaking. To move the field forward in a rational way, we need to understand the mechanism of the colloidal syntheses that do provide satisfactory results. While the precursor conversion has been studied for InN, there are many systems for which the mechanism is left unexplored. Even more problematic, the crystallization part of the mechanism has not been studied for any of the nitrides discussed here. However, the crystallization is likely the most difficult step in the whole process and thus the most critical to understand to make progress. Finally, it will be equally important that researchers treat colloidal synthesis as a true chemical reaction that has a chemical equation (which needs to be written down) and for which an accurate yield needs to be reported. By putting more rigor into writing the Experimental section, we can enhance the reproducibility of the field. Given the use of early transition metal nitrides for many applications such as catalysis, photothermal therapy, superconductors, and electrochemical capacitors, synthetic efforts should focus on providing these NCs as size-tunable colloidal particles. The field of colloidal metals nitrides is clearly challenging and still young, but adding colloidal nitrides (with synthetic control) to the portfolio of colloidal materials would open up many exciting possibilities for the future of materials science and nanotechnology.

Conflicts of interest

There are no conflicts to declare.

Acknowledgements

References

1 S. G. Kwon and T. Hyeon, *Acc. Chem. Res.*, 2008, **41**, 1696–1709.

2 Z. Hens and J. De Roo, *J. Am. Chem. Soc.*, 2020, **142**, 15627–15637.

3 E. Matijevic, *Chem. Mater.*, 1993, **5**, 412–426.

4 Z. Hens, *Science*, 2015, **348**, 1211–1212.

5 J. Park, J. Joo, S. Kwon, Y. Jang and T. Hyeon, *Angew. Chem., Int. Ed.*, 2007, **46**, 4630–4660.

6 I. Ojea-Jiménez, F. M. Romero, N. G. Bastús and V. Puntes, *J. Phys. Chem. C*, 2010, **114**, 1800–1804.

7 R. Garcia-Rodriguez, M. P. Hendricks, B. M. Cossairt, H. T. Liu and J. S. Owen, *Chem. Mater.*, 2013, **25**, 1233–1249.

8 M. Niederberger and G. Garnweitner, *Chem. – Eur. J.*, 2006, **12**, 7282–7302.

9 M. D. Tessier, K. De Nolf, D. Dupont, D. Sinnaeve, J. De Roo and Z. Hens, *J. Am. Chem. Soc.*, 2016, **138**, 5923–5929.

10 M. A. Boles, D. Ling, T. Hyeon and D. V. Talapin, *Nat. Mater.*, 2016, **15**, 141–153.

11 N. C. Anderson, M. P. Hendricks, J. J. Choi and J. S. Owen, *J. Am. Chem. Soc.*, 2013, **135**, 18536–18548.

12 J. De Roo, F. Van den Broeck, K. De Keukeleere, J. C. Martins, I. Van Driessche and Z. Hens, *J. Am. Chem. Soc.*, 2014, **136**, 9650–9657.

13 F. W. Eagle, N. Park, M. Cash and B. M. Cossairt, *ACS Energy Lett.*, 2021, 977–984.

14 J. De Roo, K. De Keukeleere, Z. Hens and I. Van Driessche, *Dalton Trans.*, 2016, **45**, 13277–13283.

15 Y. Yang, H. Qin and X. Peng, *Nano Lett.*, 2016, **16**, 2127–2132.

16 T. Kister, D. Monego, P. Mulvaney, A. Widmer-Cooper and T. Kraus, *ACS Nano*, 2018, **12**, 5969–5977.

17 J. D. Martin, *Chem. Mater.*, 2020, **32**, 3651–3656.

18 R. G. Finke, M. A. Watzky and C. B. Whitehead, *Chem. Mater.*, 2020, **32**, 3657–3672.

19 V. K. Lamer and R. H. Dinegar, *J. Am. Chem. Soc.*, 1950, **72**, 4847–4854.

20 S. Özkar and R. G. Finke, *J. Am. Chem. Soc.*, 2017, **139**, 5444–5457.

21 S. Mozaffari, W. Li, C. Thompson, S. Ivanov, S. Seifert, B. Lee, L. Kovarik and A. M. Karim, *Nanoscale*, 2017, **9**, 13772–13785.

22 B. M. McMurtry, K. Qian, J. K. Teglasi, A. K. Swarnakar, J. De Roo and J. S. Owen, *Chem. Mater.*, 2020, **32**, 4358–4368.

23 P. T. Prins, F. Montanarella, K. Dümbgen, Y. Justo, J. C. van der Bok, S. O. M. Hinterding, J. J. Geuchies, J. Maes, K. De Nolf, S. Deelen, H. Meijer, T. Zinn, A. V. Petukhov, F. T. Rabouw, C. De Mello Donega, D. Vanmaekelbergh and Z. Hens, *Nano Lett.*, 2021, **21**, 2487–2496.

24 S. Mozaffari, W. Li, M. Dixit, S. Seifert, B. Lee, L. Kovarik, G. Mpourmpakis and A. M. Karim, *Nanoscale Adv.*, 2019, **1**, 4052–4066.

25 D. R. Handwerk, P. D. Shipman, C. B. Whitehead, S. Özkar and R. G. Finke, *J. Am. Chem. Soc.*, 2019, **141**, 15827–15839.

26 M. P. Hendricks, M. P. Campos, G. T. Cleveland, I. J.-L. Plante and J. S. Owen, *Science*, 2015, **348**, 1226–1230.

27 E. Dhaene, J. Billet, E. Bennett, I. Van Driessche and J. De Roo, *Nano Lett.*, 2019, **19**, 7411–7417.

28 K. De Keukeleere, S. Coucke, E. De Canck, P. Van Der Voort, F. Delpech, Y. Coppel, Z. Hens, I. Van Driessche, J. S. Owen and J. De Roo, *Chem. Mater.*, 2017, **29**, 10233–10242.

29 D. Baranov, M. J. Lynch, A. C. Curtis, A. R. Carollo, C. R. Douglass, A. M. Mateo-Tejada and D. M. Jonas, *Chem. Mater.*, 2019, **31**, 1223–1230.

30 J. J. Calvin, J. K. Swabeck, A. B. Sedlak, Y. Kim, E. Jang and A. P. Alivisatos, *J. Am. Chem. Soc.*, 2020, **142**, 18897–18906.

31 M. R. Friedfeld, J. L. Stein, A. Ritchhart and B. M. Cossairt, *Acc. Chem. Res.*, 2018, **51**, 2803–2810.

32 M. E. Mundy, D. Ung, N. L. Lai, E. P. Jahrman, G. T. Seidler and B. M. Cossairt, *Chem. Mater.*, 2018, **30**, 5373–5379.

33 A. G. Rachkov and A. M. Schimpf, *Chem. Mater.*, 2021, **33**, 1394–1406.

34 D. R. Sadoway, *JOM*, 1991, **43**, 15–19.

35 A. MIURA, *J. Ceram. Soc. Jpn.*, 2017, **125**, 552–558.

36 K. Fung and G. Mantov, *J. Electroanal. Chem. Interfacial Electrochem.*, 1972, **35**, 27–34.

37 C. Housecroft, *Inorganic Chemistry*, Pearson, 2018, vol. 72, pp. 650–651.

38 S. H. Elder, F. J. DiSalvo, L. Topor and A. Navrotsky, *Chem. Mater.*, 1993, **5**, 1545–1553.

39 Y. Ma, L. Xiong, Y. Lu, W. Zhu, H. Zhao, Y. Yang, L. Mao and L. Yang, *Front. Chem.*, 2021, **9**, 390.

40 R. A. Karaballi, G. Humagain, B. R. A. Fleischman and M. Dasog, *Angew. Chem., Int. Ed.*, 2019, **58**, 3147–3150.

41 S. Ishii, R. P. Sugavaneshwar and T. Nagao, *J. Phys. Chem. C*, 2016, **120**, 2343–2348.

42 E. Traver, R. A. Karaballi, Y. E. Monfared, H. Daurie, G. A. Gagnon and M. Dasog, *ACS Appl. Nano Mater.*, 2020, **3**, 2787–2794.

43 R. A. Karaballi, Y. E. Monfared and M. Dasog, *Chemistry*, 2020, **26**, 8499–8505.

44 R. A. Karaballi, Y. Esfahani Monfared and M. Dasog, *Langmuir*, 2020, **36**, 5058–5064.

45 U. Guler, S. Suslov, A. V. Kildishev, A. Boltasseva and V. M. Shalaev, *Nanophotonics*, 2015, **4**, 269–276.

46 Y. Yuan, J. Wang, S. Adimi, H. Shen, T. Thomas, R. Ma, J. P. Attfield and M. Yang, *Nat. Mater.*, 2019, **19**, 282–286.

47 C. Defilippi, D. V. Shinde, Z. Dang, L. Manna, C. Hardacre, A. J. Greer, C. D'Agostino and C. Giordano, *Angew. Chem., Int. Ed.*, 2019, **58**, 15464–15470.

48 K. Momma and F. Izumi, *J. Appl. Crystallogr.*, 2011, **44**, 1272–1276.

49 A. N. Christensen, V. Romano, R. Hesse, A. F. Andresen and P. Fischer, *Acta Chem. Scand., Ser. A*, 1975, **29**, 563–564.

50 F. W. Glaser, D. Moskowitz and B. Post, *JOM*, 1953, **5**, 1119–1120.

51 K. Becker and F. Ebert, *Z. Phys.*, 1925, **31**, 268–272.

52 L. Hiltunen, M. Leskela, M. Makela, L. Niinisto, E. Nykanen and P. Soininen, *Thin Solid Films*, 1988, **166**, 149–154.

53 A. Kafizas, C. J. Carmalt and I. P. Parkin, *Coord. Chem. Rev.*, 2013, **257**, 2073–2119.

54 A. Alvarez Barragan, N. V. Ilawe, L. Zhong, B. M. Wong and L. Mangolini, *J. Phys. Chem. C*, 2017, **121**, 2316–2322.

55 K. S. Schramke, Y. X. Qin, J. T. Held, K. A. Mkhoyan and U. R. Kortshagen, *ACS Appl. Nano Mater.*, 2018, **1**, 2869–2876.

56 S. Exarhos, A. Alvarez-Barragan, E. Aytan, A. A. Balandin and L. Mangolini, *ACS Energy Lett.*, 2018, **3**, 2349–2356.

57 C. H. Winter, P. H. Sheridan, T. S. Lewkebandara, M. J. Heeg and J. W. Proscia, *J. Am. Chem. Soc.*, 1992, **114**, 1095–1097.

58 S. C. Dunn, A. S. Batsanov and P. Mountford, *J. Chem. Soc., Chem. Commun.*, 1994, 2007–2008.

59 D. C. Bradley and I. M. Thomas, *J. Chem. Soc.*, 1960, 3857–3861.

60 D. C. Bradley and E. G. Torrible, *Can. J. Chem.*, 1963, **41**, 134–138.

61 C. Lorber and L. Vendier, *Dalton Trans.*, 2013, **42**, 12203–12219.

62 A. W. Jackson and A. L. Hector, *J. Mater. Chem.*, 2007, **17**, 1016–1022.

63 C. Lorber, R. Choukroun and L. Vendier, *Eur. J. Inorg. Chem.*, 2006, 4503–4518.

64 N. Adams, H. R. Bigmore, T. L. Blundell, C. L. Boyd, S. R. Dubberley, A. J. Sealey, A. R. Cowley, M. E. G. Skinner and P. Mountford, *Inorg. Chem.*, 2005, **44**, 2882–2894.

65 A. Egeberg, O. Wenzel, R. Popescu, D. Gerthsen and C. Feldmann, *ChemistryOpen*, 2020, **10**, 334–339.

66 A. Fischer, M. Antonietti and A. Thomas, *Adv. Mater.*, 2007, **19**, 264–267.

67 J. Buha, I. Djerdj, M. Antonietti and M. Niederberger, *Chem. Mater.*, 2007, **19**, 3499–3505.

68 Y. Liu, X. Zhang, L. Lu, J. Ye, J. Wang, X. Li, X. Bai and W. Wang, *Chin. Chem. Lett.*, 2021, DOI: 10.1016/j.cclet.2021.07.054.

69 C. Giordano, C. Erpen, W. T. Yao, B. Milke and M. Antonietti, *Chem. Mater.*, 2009, **21**, 5136–5144.

70 F. D. Qu, Y. Yuan and M. H. Yang, *Chem. Mater.*, 2017, **29**, 969–974.

71 G. S. Shanker, R. Bhosale, S. Ogale and A. Nag, *Adv. Mater. Interfaces*, 2018, **5**, 1801488.

72 G. S. Shanker, G. B. Markad, M. Jagadeeswararao, U. Bansode and A. Nag, *ACS Energy Lett.*, 2017, **2**, 2251–2256.

73 D. B. O'Neill, S. K. Frehan, K. Zhu, E. Zoethout, G. Mul, E. C. Garnett, A. Huijser and S. H. C. Askes, *Adv. Opt. Mater.*, 2021, 2100510.

74 X. Kan, J. Ding, H. Zhu, C. Deng and C. Yu, *Powder Technol.*, 2017, **315**, 81–86.

75 S. Hosoya, T. Yamagishi and M. Tokonami, *J. Phys. Soc. Jpn.*, 1968, **24**, 363–367.

76 J. Gatterer, G. Dufek, P. Ettmayer and R. Kieffer, *Monatsh. Chem.*, 1975, **106**, 1137–1147.

77 Y. Liu, Q. Wu, L. Liu, P. Manasa, L. Kang and F. Ran, *J. Mater. Chem. A*, 2020, **8**, 8218–8233.

78 H. Cui, G. Zhu, X. Liu, F. Liu, Y. Xie, C. Yang, T. Lin, H. Gu and F. Huang, *Adv. Sci.*, 2015, **2**, 1500126.

79 Y. Li, J. Zhang, X. Qian, Y. Zhang, Y. Wang, R. Hu, C. Yao and J. Zhu, *Appl. Surf. Sci.*, 2018, **427**, 884–889.

80 D. Choi, G. Blomgren and P. Kumta, *Adv. Mater.*, 2006, **18**, 1178–1182.

81 T. Huang, S. Mao, G. Zhou, Z. Wen, X. Huang, S. Ci and J. Chen, *Nanoscale*, 2014, **6**, 9608.

82 D. Choi and P. N. Kumta, *J. Am. Ceram. Soc.*, 2011, **94**, 2371–2378.

83 J. H. Swisher and M. H. Read, *Metall. Trans.*, 1972, **3**, 489.

84 L. Wang, X. Zhou, N. T. Nguyen, I. Hwang and P. Schmuki, *Adv. Mater.*, 2016, **28**, 2432–2438.

85 M. H. Tsai, S. C. Sun, H. T. Chiu, C. E. Tsai and S. H. Chuang, *Appl. Phys. Lett.*, 1995, **67**, 1128–1130.

86 Y.-J. Lee, D.-Y. Kim, K.-H. Lee, M.-H. Han, K.-S. Kang, K.-K. Bae and J.-H. Lee, *Nanoscale Res. Lett.*, 2013, **8**, 128.

87 C.-T. Ho, K.-B. Low, R. F. Klie, K. Maeda, K. Domen, R. J. Meyer and P. T. Snee, *J. Phys. Chem. C*, 2010, **115**, 647–652.

88 C. F. Mallinson, B. M. Gray, A. L. Hector, M. A. McLachlan and J. R. Owen, *Inorg. Chem.*, 2013, **52**, 9994–9999.

89 A. Leineweber, H. Jacobs and S. Hull, *Inorg. Chem.*, 2001, **40**, 5818–5822.

90 F. Gillot, J. Oró-Solé and M. R. Palacín, *J. Mater. Chem.*, 2011, **21**, 9997.

91 D. C. Dunand and P. Müllner, *Adv. Mater.*, 2010, **23**, 216–232.

92 N. Gajbhiye, R. Ningthoujam and J. Weissmller, *Phys. Status Solidi A*, 2002, **189**, 691–695.

93 C. Bartholomew, *J. Catal.*, 1976, **45**, 41–53.

94 M. Shalom, V. Molinari, D. Esposito, G. Clavel, D. Ressnig, C. Giordano and M. Antonietti, *Adv. Mater.*, 2013, **26**, 1272–1276.

95 K. Xu, P. Chen, X. Li, Y. Tong, H. Ding, X. Wu, W. Chu, Z. Peng, C. Wu and Y. Xie, *J. Am. Chem. Soc.*, 2015, **137**, 4119–4125.

96 D. Gao, J. Zhang, T. Wang, W. Xiao, K. Tao, D. Xue and J. Ding, *J. Mater. Chem. A*, 2016, **4**, 17363–17369.

97 G. S. Shanker and S. Ogale, *ACS Appl. Energy Mater.*, 2021, **4**, 2165–2173.

98 M. J. Winiarski, *J. Solid State Chem.*, 2018, **266**, 161–165.

99 D. Bocharov, A. Anspoks, J. Timoshenko, A. Kalinko, M. Krack and A. Kuzmin, *Radiat. Phys. Chem.*, 2020, **175**, 108100.

100 A. Zakutayev, C. M. Caskey, A. N. Fioretti, D. S. Ginley, J. Vidal, V. Stevanovic, E. Tea and S. Lany, *J. Phys. Chem. Lett.*, 2014, **5**, 1117–1125.

101 T. Maruyama and T. Morishita, *Appl. Phys. Lett.*, 1996, **69**, 890–891.

102 W. Zhu, X. Zhang, X. Fu, Y. Zhou, S. Luo and X. Wu, *Phys. Status Solidi A*, 2012, **209**, 1996–2001.

103 Z. Yin, C. Yu, Z. Zhao, X. Guo, M. Shen, N. Li, M. Muzzio, J. Li, H. Liu, H. Lin, J. Yin, G. Lu, D. Su and S. Sun, *Nano Lett.*, 2019, **19**, 8658–8663.

104 C. Panda, P. W. Menezes, M. Zheng, S. Orthmann and M. Driess, *ACS Energy Lett.*, 2019, **4**, 747–754.

105 P. X. Xi, Z. H. Xu, D. Q. Gao, F. J. Chen, D. S. Xue, C. L. Tao and Z. N. Chen, *RSC Adv.*, 2014, **4**, 14206–14209.

106 U. Hahn and W. Weber, *Phys. Rev. B: Condens. Matter Mater. Phys.*, 1996, **53**, 12684–12693.

107 F. Gulo, A. Simon, J. Kohler and R. K. Kremer, *Angew. Chem., Int. Ed.*, 2004, **43**, 2032–2034.

108 X. Y. Cui, A. Soon, A. E. Phillips, R. K. Zheng, Z. W. Liu, B. Delley, S. P. Ringer and C. Stampfl, *J. Magn. Magn. Mater.*, 2012, **324**, 3138–3143.

109 J. Choi and E. G. Gillan, *Inorg. Chem.*, 2005, **44**, 7385–7393.

110 M. Birkett, C. N. Savory, A. N. Fioretti, P. Thompson, C. A. Muryn, A. D. Weerakkody, I. Z. Mitrovic, S. Hall, R. Treharne, V. R. Dhanak, D. O. Scanlon, A. Zakutayev and T. D. Veal, *Phys. Rev. B*, 2017, **95**, 115201.

111 U. Zachwieja and H. Jacobs, *J. Less-Common Met.*, 1990, **161**, 175–184.

112 H. Jacobs and U. Zachwieja, *J. Less-Common Met.*, 1991, **170**, 185–190.

113 R. Juza and H. Hahn, *Z. Anorg. Allg. Chem.*, 1939, **241**, 172–178.

114 G. Paniconi, Z. Stoeva, H. Doberstein, R. I. Smith, B. L. Gallagher and D. H. Gregory, *Solid State Sci.*, 2007, **9**, 907–913.

115 D. Wang and Y. Li, *Chem. Commun.*, 2011, **47**, 3604–3606.

116 D. Flaxbart, *J. Am. Chem. Soc.*, 1999, **121**, 2339–2339.

117 H. Wu and W. Chen, *J. Am. Chem. Soc.*, 2011, **133**, 15236–15239.

118 D. D. Vaughn Ii, J. Araujo, P. Meduri, J. F. Callejas, M. A. Hickner and R. E. Schaak, *Chem. Mater.*, 2014, **26**, 6226–6232.

119 R. W. Lord, C. F. Holder, J. L. Fenton and R. E. Schaak, *Chem. Mater.*, 2019, **31**, 4605–4613.

120 D. Barman, S. Paul, S. Ghosh and S. K. De, *ACS Appl. Nano Mater.*, 2019, **2**, 5009–5019.

121 R. Kadzutu-Sithole, L. F. E. Machogo-Phao, T. Kolokoto, M. Zimuwandeyi, S. S. Gqoba, K. P. Mubiayi, M. J. Moloto, J. V. Wyk and N. Moloto, *RSC Adv.*, 2020, **10**, 34231–34246.

122 S. Mondal and C. R. Raj, *J. Phys. Chem. C*, 2018, **122**, 18468–18475.

123 T. Nakamura, H. Hayashi, T. A. Hanaoka and T. Ebina, *Inorg. Chem.*, 2014, **53**, 710–715.

124 R. K. Sithole, L. F. E. Machogo, M. A. Airo, S. S. Gqoba, M. J. Moloto, P. Shumbula, J. Van Wyk and N. Moloto, *New J. Chem.*, 2018, **42**, 3042–3049.

125 R. Deshmukh, G. B. Zeng, E. Tervoort, M. Staniuk, D. Wood and M. Niederberger, *Chem. Mater.*, 2015, **27**, 8282–8288.

126 A. Egeberg, L. Warmuth, S. Riegsinger, D. Gerthsen and C. Feldmann, *Chem. Commun.*, 2018, **54**, 9957–9960.

127 R. Deshmukh, E. Tervoort, J. Kach, F. Rechberger and M. Niederberger, *Dalton Trans.*, 2016, **45**, 11616–11619.

128 Y. Liu, D. Lin, P. Y. Yuen, K. Liu, J. Xie, R. H. Dauskardt and Y. Cui, *Adv. Mater.*, 2017, **29**, 1605531.

129 J. Livage, C. Sanchez, M. Henry and S. Doeuff, *Solid State Ionics*, 1989, **32–33**, 633–638.

130 D. Partin, D. Williams and M. O'Keeffe, *J. Solid State Chem.*, 1997, **132**, 56–59.

131 N. C. Coronel, Ph.D. thesis, 2016.

132 T. Yang, Z. Zhang, Y. Li, M. Lv, S. Song, Z. Wu, J. Yan and S. Han, *Appl. Surf. Sci.*, 2009, **255**, 3544–3547.

133 K. Kuriyama, Y. Takahashi and F. Sunohara, *Phys. Rev. B: Condens. Matter Mater. Phys.*, 1993, **48**, 2781–2782.

134 F. Zong, H. Ma, J. Ma, W. Du, X. Zhang, H. Xiao, F. Ji and C. Xue, *Appl. Phys. Lett.*, 2005, **87**, 233104.

135 S. Prabha, D. Durgalakshmi, K. Subramani, P. Aruna and S. Ganesan, *ACS Appl. Mater. Interfaces*, 2020, **12**, 19245–19257.

136 P. N. Taylor, M. A. Schreuder, T. M. Smeeton, A. J. D. Grundy, J. A. R. Dimmock, S. E. Hooper, J. Heffernan and M. Kauer, *J. Mater. Chem. C*, 2014, **2**, 4379–4382.

137 A. H. Jayatissa, T. Wen and M. Gautam, *J. Phys. D: Appl. Phys.*, 2012, **45**, 045402.

138 G. Paniconi, Z. Stoeva, R. I. Smith, P. C. Dippo, B. L. Gallagher and D. H. Gregory, *J. Solid State Chem.*, 2008, **181**, 158–165.

139 F. Zong, H. Ma, C. Xue, W. Du, X. Zhang, H. Xiao, J. Ma and F. Ji, *Mater. Lett.*, 2006, **60**, 905–908.

140 R. Ahumada-Lazo, S. M. Fairclough, S. J. O. Hardman, P. N. Taylor, M. Green, S. J. Haigh, R. Saran, R. J. Curry and D. J. Binks, *ACS Appl. Nano Mater.*, 2019, **2**, 7214–7219.

141 H. Amano, N. Sawaki, I. Akasaki and Y. Toyoda, *Appl. Phys. Lett.*, 1986, **48**, 353–355.

142 M. Kaur, K. Singh, P. Singh, A. Kaur, R. Meena, G. P. Singh, H. Barabadi, M. Saravanan and A. Kumar, *Nanomed. J.*, 2020, **7**, 194–198.

143 Y. Bian, M. Liu, G. Ke, Y. Chen, J. DiBattista, E. Chan and Y. Yang, *Surf. Coat. Technol.*, 2015, **267**, 65–69.

144 C. Li, X. Liu, L. Shu and Y. Li, *Mater. Express*, 2015, **5**, 367–370.

145 C. Li, X.-Z. Liu, B. Peng, L. Shu and Y.-R. Li, *Rare Met.*, 2016, **35**, 408–411.

146 V. Kudyakova, R. Shishkin, A. Elagin, M. Baranov and A. Beketov, *J. Eur. Ceram. Soc.*, 2017, **37**, 1143–1156.

147 G. G. Arizaga, M. J. Oviedo and O. E. Lopez, *Colloids Surf., B*, 2012, **98**, 63–71.

148 P. Antoniammal and D. Arivuoli, *J. Nanomater.*, 2012, **2012**, 1–11.

149 S. Nakamura and G. Fasol, *The Blue Laser Diode*, Springer Berlin Heidelberg, 1997, pp. 313–315.

150 E. Starikov, P. Shiktorov, V. Gružinskis, L. Reggiani, L. Varani, J. Vaissière and J. H. Zhao, *Phys. B*, 2002, **314**, 171–175.

151 H. Neff, O. Semchinova, A. Lima, A. Filimonov and G. Holzhueter, *Sol. Energy Mater. Sol. Cells*, 2006, **90**, 982–997.

152 H. P. T. Nguyen, Y.-L. Chang, I. Shih and Z. Mi, *IEEE J. Sel. Top. Quantum Electron.*, 2011, **17**, 1062–1069.

153 J. Wu, *J. Appl. Phys.*, 2009, **106**, 011101.

154 Z. H. Liu and R. Beaulac, *Chem. Mater.*, 2017, **29**, 7507–7514.

155 Z. Liu, L. M. Janes, M. Saniepay and R. Beaulac, *Chem. Mater.*, 2018, **30**, 5435–5443.

156 B. Schwenzer, L. Loeffler, R. Seshadri, S. Keller, F. F. Lange, S. P. DenBaars and U. K. Mishra, *J. Mater. Chem.*, 2004, **14**, 637.

157 G. Sinha, S. K. Panda, P. Mishra, D. Ganguli and S. Chaudhuri, *J. Phys.: Condens. Matter*, 2007, **19**, 346209.

158 Y. Chen, N. Jyoti and J. Kim, *Appl. Phys. A*, 2010, **102**, 517–519.

159 Y. Chen, M. Maniruzzaman and J. Kim, *Int. J. Precis. Eng. Manuf.*, 2011, **12**, 573–576.

160 H. Xiao, H. Pei, J. Liu, J. Cui, B. Jiang, Q. Hou and W. Hu, *Mater. Lett.*, 2012, **71**, 145–147.

161 H. Yan, K. Liu, R. Luo, S. Chen and H. Cao, *Mater. Lett.*, 2010, **64**, 2109–2111.

162 P. G. Li, M. Lei, Y. X. Du, X. Guo and W. H. Tang, *Appl. Surf. Sci.*, 2009, **255**, 3843–3847.

163 A. Manz, A. Birkner, M. Kolbe and R. A. Fischer, *Adv. Mater.*, 2000, **12**, 569–573.

164 L. Grocholl, J. J. Wang and E. G. Gillan, *Chem. Mater.*, 2001, **13**, 4290–4296.

165 F. Kawamura, K. Watanabe, T. Takeda and T. Taniguchi, *J. Cryst. Growth*, 2011, **321**, 100–105.

166 J. F. Janik and R. L. Wells, *Chem. Mater.*, 1996, **8**, 2708–2711.

167 O. I. Micic, S. P. Ahrenkiel, D. Bertram and A. J. Nozik, *Appl. Phys. Lett.*, 1999, **75**, 478–480.

168 H. F. Gaiser, R. Popescu, D. Gerthsen and C. Feldmann, *Chem. Commun.*, 2020, **56**, 2312–2315.

169 S. D. Dingman, N. P. Rath, P. D. Markowitz, P. C. Gibbons and W. E. Buhro, *Angew. Chem., Int. Ed.*, 2000, **39**, 1470–1472.

170 J. Choi and E. G. Gillan, *J. Mater. Chem.*, 2006, **16**, 3774–3784.

171 A. P. Purdy, *Inorg. Chem.*, 1994, **33**, 282–286.

172 C. Wu, T. Li, L. Lei, S. Hu, Y. Liu and Y. Xie, *New J. Chem.*, 2005, **29**, 1610.

173 J. C. Hsieh, D. S. Yun, E. Hu and A. M. Belcher, *J. Mater. Chem.*, 2010, **20**, 1435.

174 P. K. Palomaki, E. M. Miller and N. R. Neale, *J. Am. Chem. Soc.*, 2013, **135**, 14142–14150.

175 L. Wang, Q. Shen, D. Zhao, J. Lu, W. Liu, J. Zhang, K. Bao and Q. Zhou, *J. Cryst. Growth*, 2017, **471**, 62–65.

176 N. S. Karan, Y. Chen, Z. Liu and R. Beaulac, *Chem. Mater.*, 2016, **28**, 5601–5605.

177 Y. Chen, N. T. Landes, D. J. Little and R. Beaulac, *J. Am. Chem. Soc.*, 2018, **140**, 10421–10424.

178 K. Sardar, M. Dan, B. Schwenzer and C. N. R. Rao, *J. Mater. Chem.*, 2005, **15**, 2175–2177.

179 B. Chitara, D. J. Late, S. B. Krupanidhi and C. N. R. Rao, *Solid State Commun.*, 2010, **150**, 2053–2056.

180 Y. C. Choi, H. Kim, C. Lee, J. Son, H. Baik, S. Park, J. Kim and K. S. Jeong, *Chem. Mater.*, 2019, **31**, 5370–5375.